Full-Potential Simulation of X-ray Raman Scattering Spectroscopy

Yves Joly,*,[†] Chiara Cavallari,[‡] Sergey A. Guda,[§] and Christoph J. Sahle[‡]

[†]Univ. Grenoble Alpes & CNRS, Institut NÉEL, F-38042 Grenoble, France
[‡]European Synchrotron Radiation Facility, BP 220, F-38043 Grenoble Cedex, France
[§]Institute for Mathematics, Mechanics, and Computer Science, Southern Federal University, 344090 Rostov-on-Don, Russia

ABSTRACT: We present a new ab initio way to calculate X-ray Raman scattering spectra within the independent electron approximation. Our approach avoids any approximation about the shape of the used potential and leads to good agreement between experiment and theory. We show that the momentum transfer dependence in two typical cases, the F K-edge in LiF and the B and N K-edges in hexagonal BN, is well-reproduced. A more in-depth analysis of the electronic states and of the local atomic structure around the absorbing atoms is at hand.
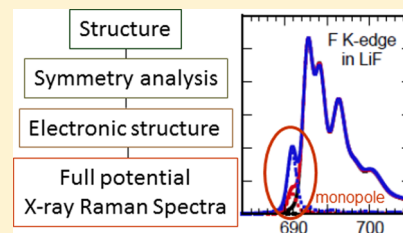
1. INTRODUCTION

Unraveling the electronic and local atomic structure is a mandatory step to understand the properties of matter. For this purpose, especially for disordered systems such as liquids and glasses, X-ray absorption spectroscopy (XAS) has been tremendously useful. However, in many cases the absorbing sample environment, for example used to create extreme conditions, or even the self-absorption in the sample itself renders the investigation of absorption edges of light elements very difficult. In these cases, nonresonant inelastic X-ray scattering (NIXS or NRIXS), which uses the energy loss between *in*coming and *out*going hard X-rays, becomes help-ful.[1,2] It is a part of all of the inelastic X-ray scattering processes, which also include resonant inelastic X-ray scattering (RIXS). In the present paper, we are specifically concerned with the energy loss resulting from an electronic transition from a core state up to the conduction band, so closely connected to the absorption edges seen in XAS. In this case, the X-ray Raman scattering (XRS) terminology is most often used, and we will keep this last acronym in the following. From the first XRS experiments, performed by Suzuki and collaborators at the end of the 1960s,[3,4] a vast improvement of this nonresonant inelastic scattering technique has been achieved, with the development of new spectrometers at different synchrotron beamlines[5−8] with increased detection power as well as energy and angular resolution.[9] In addition to the access to low-energy edges, XRS has the property that it depends on the momentum transfer, **q**, between the incoming and outgoing beams. Thanks to the recent experimental improvements, the sensitivity to this term enriches the overview of the electronic states around the absorbing atoms.[10]

The purpose of this paper is to present a new way to simulate XRS spectra using first-principles theory and to give examples of information that we can obtain in this way from the investigated materials. We use a density functional theory (DFT) approach, and we already know from the X-ray absorption near edge structure (XANES) that this theory is convenient for simulating the K-edges of all of the elements and the L$_{23}$ edges of the heavy ones. This restriction makes our method complementary to the multiplet ligand field theory already used for example by Gordon et al.[11] to simulate XRS or to the related but less used effective operator approach of van Veenendaal and Haverkort.[12] These methods are very specifically devoted to highly localized states and never to the main dipole component at K-edges.

DFT simulations are already possible. They use a plane-wave pseudopotential framework,[13] transition potential approxima-tion,[14,15] or the more user-friendly multiple scattering theory[10] but are limited to potentials described within the muffin-tin approximation that is spherical inside the atoms and constant between them. FDMNES[16] is a self-consistent ab initio code that is already extensively used to simulate XANES and resonant elastic X-ray scattering (REXS). Its full-potential approach makes it especially precise for simulating absorption edges of light elements often embedded in nondense surroundings or within low symmetry. On the other side, its calculation method is relativistic, and the heaviest chemical elements are also accessible. Finally, XRS, like XANES, is only poorly sensitive to the band gap or to the thinnest features specific from correlated materials. All of this makes our method suitable for all kinds of materials without any restrictions.

The paper is organized as follows. In section 2 we give the main theoretical ingredients of XRS. Section 3 is devoted to the implementation in the FDMNES code and to the character-istics of the calculation. Finally, in section 4 we present two applications, showing comparisons between experimental data and simulated spectra of the F K-edge in LiF and the N and B K-edges in h-BN.

2. THEORY

2.1. XRS Formulation. Most of the theory can already be found in papers[17] or textbooks.[1] Therefore, in this context we just recall the basic relations of XRS. The double differential

scattering cross section derived from a first-order perturbation treatment of a scattering event connected with the transition of the electron system from its ground state $|i\rangle$ into a final state $|f\rangle$ is given by

$$\frac{d^2\sigma}{d\Omega_2 d\hbar\omega_2} = r_0^2 \frac{\omega_2}{\omega_1} |\epsilon_1 \cdot \epsilon_2|^2 \, S(\mathbf{q}, \omega) \tag{1}$$

where $\epsilon_{1(2)}$ and $\hbar\omega_{1(2)}$ stand for the incoming (outgoing) beam polarizations and energies, respectively, whereas $\hbar\omega = \hbar(\omega_2 - \omega_1)$ is the energy transfer. The momentum transfer $\mathbf{q} = \mathbf{k}_2 - \mathbf{k}_1$, where $\mathbf{k}_{1(2)}$ is the momentum of the incoming (outgoing) photon beam, is given in reciprocal space units. r_0 is the electron radius, and the dynamic structure factor S is given by

$$S(\mathbf{q}, \omega) = \sum_{i,f} |\langle f| e^{-i\mathbf{q}\cdot\mathbf{r}} |i\rangle|^2 \delta(\hbar\omega - E_f + E_i) \tag{2}$$

where E_i and E_f are the energies of the core (initial) and excited (final) states of the material. We have directly written the formula within a monoelectronic approach, thereby avoiding a summation over all of the electrons of the system.

It is straightforward to observe that when a first-order expansion of the exponential in eq 2 ($e^{-i\mathbf{q}\cdot\mathbf{r}} = 1 - i\mathbf{q}\cdot\mathbf{r}$) is used and the *near* orthogonality of the core and valence wave functions (they are solutions of *nearly* the same Hamiltonian for core spectroscopies) is taken into account, in the limit of small $\mathbf{q}$, S is simply proportional to the absorption cross section within the dipole approximation, with $\mathbf{q}$ playing the role of the polarization in XAS.

The $\mathbf{q}$ dependence seen in many experiments nevertheless needs a more precise description of the transition operator. To this end, we use the relation

$$e^{-i\mathbf{q}\cdot\mathbf{r}} = 4\pi \sum_{l,m} (-i)^l j_l(qr) Y_l^{m*}(\hat{r}) Y_l^m(\hat{q}) \tag{3}$$

where q and r are the moduli of $\mathbf{q}$ and $\mathbf{r}$, respectively, $\hat{q}$ and $\hat{r}$ are the angles representing the momentum transfer and position, respectively, and the j_l are Bessel functions. Introducing this expansion in eq 2, one gets

$$S(\mathbf{q}, \omega) = \sum_{i,f} |\sum_l M_{if,l}|^2 \delta(\hbar\omega - E_f + E_i) \tag{4}$$

where

$$
\begin{aligned}
M_{if,0} &= \langle f| j_0(qr) |i\rangle \\
M_{if,l} &= 4\pi(-i)^l \sum_{-l \le m \le l} Y_l^m(\hat{q}) \langle f| j_l(qr) Y_l^{m*}(\hat{r}) |i\rangle .
\end{aligned}
\tag{5}
$$

In the above expression, the $l = 1$ term, to first order, leads to the dominating dipole component: $j_1(qr) = -\cos(qr)/(qr) + \sin(qr)/(qr)^2 \approx \frac{1}{3} qr$. With increasing qr, higher-order terms in the expansion gain weight, and new excitation channels with $l \ne 1$ open up, leading to the 2^l-pole transition channels. Very interestingly, for $l = 0$ to second order we have $j_0(qr) = \sin(qr)/(qr) \approx 1 - \frac{1}{6}(qr)^2$, and contrary to XAS, the r^2 term makes this so-called monopole contribution nonzero. The $\Delta l = 0$ selection rule in the transition between the core and valence states then follows. Consequently, at the K-edge, for instance, it probes the s states, whereas the dipole transition probes the p states. Likewise for $l = 2$ one gets quadrupole transitions, for $l = 3$ octupole transitions, and so on. The richness of the $\mathbf{q}$-dependent analysis lies in a more complete understanding of the projection of the density of states onto the absorbing atoms.

2.2. Expansion in the Atomic Basis. Upon comparison of the XAS and XRS formulas, except for the prefactor, the only difference is the different transition operators. In XANES it is given, up to the electric quadrupole term, by $o = \epsilon \cdot \mathbf{r}(1 + \frac{i}{2}\mathbf{k}\cdot\mathbf{r} + ...)$, where $\mathbf{k}$ is the electromagnetic wave vector, whereas in XRS one uses the expansion in eq 3. In the atoms, we use the expansions in spherical harmonics for the core and final states:[18]

$$\varphi_{i(f)} = \sum_{L,\sigma} a_{L\sigma}^{i(f)} b_{L\sigma}^{i(f)}(r) Y_l^m(\hat{r}) \chi_\sigma \tag{6}$$

where σ is the spin and $L = (l, m, s)$. Following Wood and Boring,[19] we have used the (l, m, s) basis instead of the more classical $(l, J_\pm, J_z)$ quantum numbers, and $s = \pm\frac{1}{2}$ is the index of the two solutions of the radial relativistic Schrödinger equation, $b_{L\sigma}$. When spin−orbit splitting is omitted, s and σ merge. $a_{L\sigma}^{i(f)} = a_{l,m+\sigma-s,s}^{i(f)}$ is the amplitude, and χ_σ is the spin projector. For the core, the $a_{L\sigma}^i$ are nonzero for a single l_i value corresponding to the edge and such that the state is normalized to 1, whereas the $a_{L\sigma}^f$ are related to the density of the valence states. They are also related to the multiple scattering amplitudes $\tau_{LL'\sigma}$ by

$$\frac{1}{2}(\tau_{LL'\sigma} - \tau_{L'L\sigma}^*) = \hat{\tau}_{LL'\sigma} = -i \sum_f a_{L\sigma}^f a_{L'\sigma}^{f*} \tag{7}$$

Each of the matrix elements thus becomes

$$M_{if,l} = 4\pi(-i)^l \sum_{-l \le m \le l} Y_l^m(\hat{q}) \times \sum_{L_i,L_f,\sigma} a_{L_f\sigma}^{f*} a_{L_i\sigma}^i R_{L_iL_f}^{l\sigma} \Gamma_{L_iL_f}^{lm} \tag{8}$$

In eq 8, the angular integral, or Gaunt coefficient, is given by

$$\Gamma_{L_iL_f}^{lm} = \int Y_{l_i}^{m_i*} Y_l^m Y_{l_f}^{m_f} \, d\hat{r} \tag{9}$$

leading to the selection rules. The radial integral is

$$R_{L_iL_f}^{l\sigma} = \int b_{L_f\sigma}(r) b_{L_i\sigma}(r) j_l(qr) r \, dr \tag{10}$$

The only differences compared to XAS are thus first that r^l is substituted by j_l in the radial integral and second that the angular terms and their summations are slightly different.

Introducing all of these terms into eq 4, one gets

$$
\begin{aligned}
S(\mathbf{q}, \omega) = \sum_{i,L_i,\sigma} (4\pi a_{L_i\sigma}^i)^2 \sum_{l,m,l',m'} i^{l-l'+1} Y_l^{m*}(\hat{q}) Y_{l'}^{m'}(\hat{q}) \times \\
\sum_{L_f,L_f'} R_{L_iL_f}^{l\sigma} R_{L_iL_f'}^{l'\sigma} \Gamma_{L_iL_f}^{lm} \Gamma_{L_iL_f'}^{l'm'} \hat{\tau}_{L_fL_f'\sigma} \times \delta(\hbar\omega - E_f + E_i)
\end{aligned}
\tag{11}
$$

where each core state i has at most two components of different spin states, which makes its contribution diagonal.

One can also note that for disordered materials (i.e., averaging over the incidence angles and thus the $\mathbf{q}$ directions), the orthogonality of the spherical harmonics limits the double summation over l, m and l', m' to its diagonal terms, and the products $i^{l-l'} Y_l^{m*}(\hat{q}) Y_{l'}^{m'}(\hat{q})$ may simply be skipped. Consequently, as in XAS, one does not get crossed multipole terms.

3. IMPLEMENTATION

The FDMNES code is an ab initio software that allows simulation of X-ray absorption spectroscopy as well as resonant and nonresonant X-ray scattering spectroscopies. One of its main characteristics is that two different techniques can be independently used to solve the electronic structure. The full-potential finite difference method (FDM) precisely applies for arbitrarily shaped potentials,[20] while full multiple scattering theory (MST) gives rise to less precise but faster calculations. As stated in the Introduction, calculations can be applied for all classes of materials, and it is especially efficient for the K-edges of all of the elements and the $L_{2,3}$ edges of the heavy ones. It should nevertheless be noted that a time-dependent DFT (TD-DFT) extension expands the scope of the software to the other edges.[21] Importantly a recent numerical development in FDMNES within the FDM framework[22] makes this code up to 40 times faster than it was before. The response functions of most materials can thus now be computed on conventional personal computers.

The main steps in an FDMNES simulations, illustrated Figure 1, are the following. First, from the unit cell (or
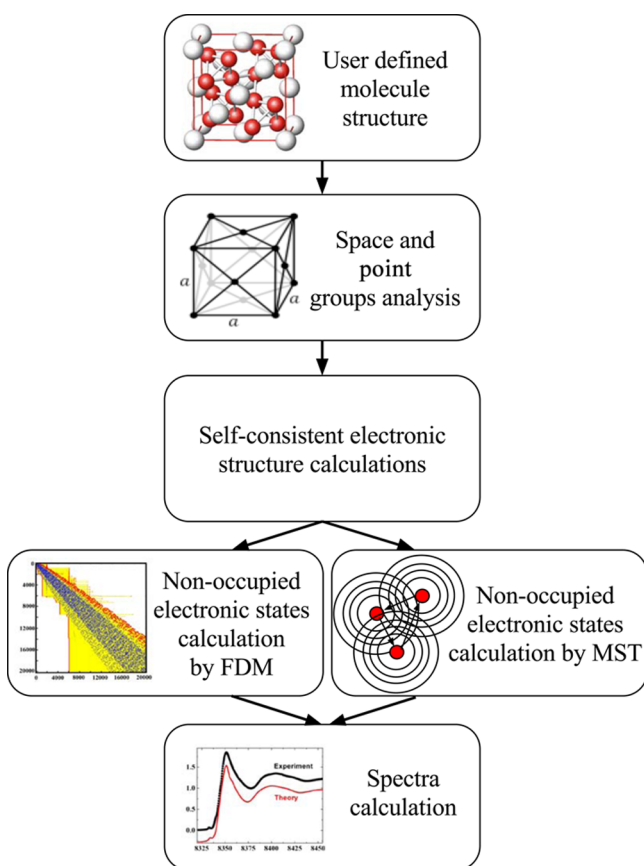

Figure 1. Flowchart of FDMNES. The different steps are automatically performed.

molecule) structure given by the user, the code performs an analysis of the space and point groups to get the equivalent and nonequivalent atoms. Second, the code makes independent self-consistent calculations of the electronic structure around all of the nonequivalent absorbing atoms. It uses a cluster approach, limiting the simulation to all of the atoms inside a sphere that is often but not necessarily centered around the absorbing atoms. The necessary cluster radius is typically in the

range of 5−7 Å but is sometimes greater for highly symmetric structures. Third, the nonoccupied electronic states are calculated using the resulting potential over the entire energy range probed by the photoelectron. It is at this step that using the FDM we directly solve the relativistic or nonrelativistic Schrödinger equation on a grid of points and get as solutions all of the final-state amplitudes of the wave functions on these grid points expressed in the spherical harmonic basis of the atoms. From eq 7 they lead to $\hat{\tau}_{L_jL_j'\sigma}$. Equation 11 for $S(\mathbf{q}, \omega)$ is thus general using either FDM or MST. The f states are defined from the outer sphere using the spherical solutions in vacuum (Bessel and Hankel functions) and not plane waves. The number of elements in this basis depends on the sphere radius. Finally, a Lorentzian convolution to account for the core hole and photoelectron state width is performed, optionally followed by a Gaussian convolution to account for the experimental resolution, and the total signal with its multipole expansion is obtained by summation of the contributions from all of the absorbing atoms of the molecule or the unit cell. By default the core hole is included only in the third step, but an option that is sometimes necessary for insulating materials allows its introduction also in the second step.

It should be noted that all of these steps are automatic, with the user giving only the atomic structure, the energy range to calculate, the wanted edge, and a specific keyword to choose the FDM or MST simulation technique. This is the point that makes the code especially user-friendly.

4. APPLICATION

4.1. Experiments. All of the experimental data were collected at beamline ID20 of the ESRF. Photons from four U26 undulators were monochromatized first by a cryogenically cooled Si(111) double-crystal monochromator followed by a Si(311) channel-cut monochromator. By means of mirrors in the Kirkpatrick−Baez geometry, the incident X-ray photons were focused to a spot size of 10 μm × 20 μm (V × H) at the sample position, which was located at approximately 65 m from the source. We used the large-solid-angle XRS spectrometer employing 36 spherically bent Si(660) (bending radius of 1 m) for the energy and momentum analysis of the inelastically scattered photons. The analyzer crystals are arranged in three groups of 12 crystals in the vertical scattering plane, where the groups have mean scattering angles of 40°, 80°, and 120°, respectively. For the final q-dependent spectra we averaged signals from three analyzer crystals with equal momentum transfer, giving rise to momentum transfers between 3.0 and 9.0 Å^{-1}. We used the XRStools program package to analyze all of the experimental data.[2] The overall energy resolution was 0.7 eV. The samples (LiF and h-BN, both obtained from Sigma-Aldrich and used without further processing) were finely ground to powder and pressed into small pellets.

4.2. Results on LiF. LiF is a cubic system with space group $Fm\bar{3}m$ and a = 4.0351 Å. There are four equivalent LiF molecules in the unit cell, and the F point group is $m3m$. It is thus a highly symmetric system. We performed self-consistent field (SCF) simulations for clusters with radii of up to 8 Å, where convergence was achieved. We found slightly better results when the core hole was included in the SCF. After the main calculation, the simulated spectra were convoluted by a Lorentzian function whose width is a sum of two terms. The first term is related to the core-hole lifetime and is Γ_H = 0.21 eV for the F K-edge. The second term corresponds to all of the

inelastic processes of the photoelectron. By default FDMNES uses a simple arctangent model versus photoelectron energy ranging from 0 eV at the Fermi energy up to a maximum value Γ_m at high energy. Here we chose $\Gamma_m = 5$ eV. Finally, a Gaussian broadening with a full width at half-maximum (fwhm) of $\Gamma_a = 1.1$ eV was applied to account for the finite experimental resolution.

In Figure 2 we show the agreement between the simulation performed using the full-potential FDM approach and the
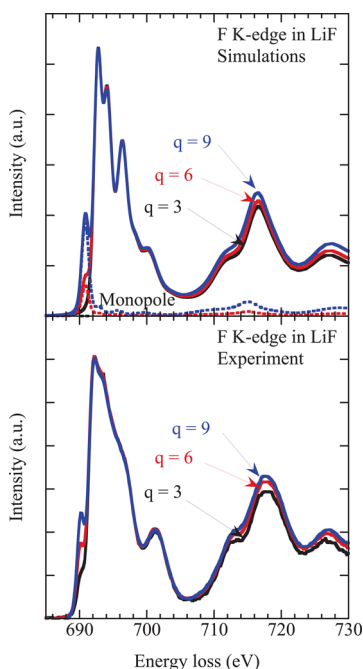
Figure 2. XRS spectra of the F K-edge in LiF for $q = 3$, 6, and 9 Å^{-1}: (bottom) experimental spectra; (top) simulations. Dotted lines show the monopole contribution, which increases with increasing q. To better highlight the change with q, the data and simulated spectra were normalized to the main peak at 692.5 eV, which has mainly dipole character. The effect of the monopole term is evidenced by the first feature at 690 eV but also contributes at higher energy, where it is responsible for the slight increase in intensity.

experiment at the F K-edge. We recover the results already found at this edge by Hämäläinen and collaborators.[13] It is good for the general shape and the main feature positions. To see better the change in the monopole term with the three values of q (3, 6, and 9 Å^{-1}), the data and simulated spectra were normalized to the main peak at 692.5 eV. The monopole contribution explains the pre-edge peak at 690 eV. This feature is thus a pure s state. The monopole also gives a contribution beyond 710 eV that explains the smooth increase in the intensity with increasing q. The quadrupole contribution was included in the simulation, but it is very small.

By comparison with a calculation using the multiple scattering approach within the muffin-tin approximation for the potential shape (all other parameters being the same), one can check in Figure 3 that the agreement is better using FDM. The amplitude of the main peak at 692.5 eV is better reproduced, and the monopole contribution is well-resolved. MST does not give a clear pre-edge feature, and we thus see that even in a highly symmetric system the full-potential approach leads to better agreement between experiment and theory.
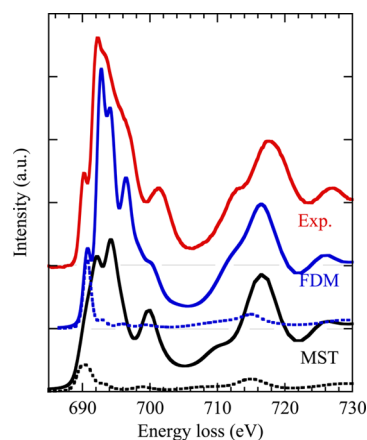

Figure 3. Comparison of the XRS spectra at the F K-edge in LiF for $q = 9$ Å^{-1} using the FDM and MST/muffin-tin approaches. The bottom curve is the MST simulation, in the middle the FDM simulation, and at the top the experiment. In the lowest-energy part of the spectra, the full-potential FDM shows better agreement with experiment, and the monopole component (dotted line) is well-reproduced.

4.3. Results on h-BN. To perform the simulations on h-BN we used the Wyckoff structure.[23] Its space group is $P63/mmc$ with $a = 2.50399$ Å and $c = 6.6612$ Å, and there are two equivalent BN molecules per unit cell. For both atoms the point group is $\bar{6}m2$. In the same way as with LiF, we performed SCF simulations for clusters with radii of up to 8 Å at the B edge and 10 Å at the N edge, where convergence was more difficult to achieve. As for LiF, SCF was performed with the core hole included. For the convolution we used $\Gamma_H = 0.15$ and 0.18 eV for B and N, respectively. We again chose $\Gamma_m = 5$ eV, but we used a Gaussian broadening of $\Gamma_a = 0.3$ eV, which is lower than for LiF.

As shown in Figure 4, the general shape and the main feature positions from the FDM simulation and the experiment at the boron K-edge are in good agreement, slightly better than in the previous study by Feng et al.[24] We also found that the monopole contribution increases with increasing q. Interestingly, it can be seen that there is no monopole contribution in the first peak at 192 eV. This feature is thus a pure 2p state, and as in the case of LiF, we chose it to normalize the different spectra. It can be clearly seen that the change in the second peak is mainly due to the monopole contribution. As observed for LiF, the quadrupole contribution is very small.

We used the same normalization procedure at the nitrogen K-edge because again the first feature has pure dipole character. At this edge the agreement is not excellent, especially in the lowest-energy part of the edge (Figure 5), but nevertheless the main features are there. We attribute the shoulder located at 406 eV with increasing q to the monopole contribution.

Looking at the structure and the density of states given by the code makes the spectroscopic analysis straightforward. The lowest-energy peak in the N and B K-edges corresponds to the antibonding N-p_z–B-p_z σ^* level, seen respectively from the N and B sides. The basal symmetry plane makes the atomic s–p_z hybridization impossible, which explains the lack of monopole contributions at the corresponding energy.

On the contrary, because of the threefold axis, the p_x and p_y states are sp^2-hybridized when forming a band with their neighbors. A monopole peak is thus visible at the second feature in both edges. It should also be noted that because the interatomic distances in the basal plane are smaller than those
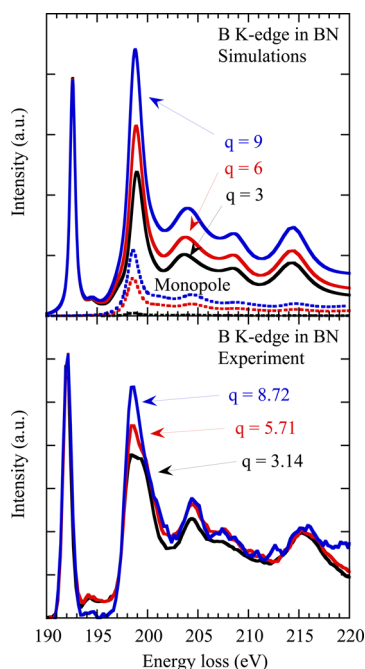
Figure 4. XRS spectra at the B K-edge in BN for three values of the momentum transfer q: (bottom) experimental data; (top) simulations. Dotted lines show the monopole contribution, which increases with increasing q. To clearly see the change with q, the data and simulated spectra were normalized to the first peak at 192 eV, which is only of dipole origin. The effect of the monopole term can be seen in the feature located at 199 eV and also in contribution at higher energy.
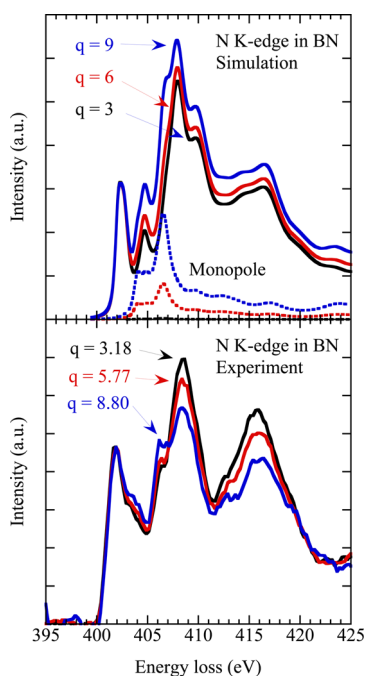

Figure 5. XRS spectra at the N K-edge in BN for three values of the momentum transfer q: (bottom) experimental data; (top) simulations. Dotted lines show the monopole contribution, which increases with increasing q. To observe clearly the change with q, the data and simulated spectra were normalized to the first peak, located at 402 eV, which is only dipole. The effect of the monopole term is evidenced by the shoulder at 406 eV.

in the plane along the c axis, it is well expected that the corresponding N-sp^2–B-sp^2 antibonding molecular orbital lies at higher energy. Finally, the very low contribution of the quadrupole is simply due to the low atomic number of the absorbing atoms, resulting in a very low amplitude of their nonlocalized d states.

5. CONCLUSION

We have shown that good agreement with XRS data can be obtained using an ab initio DFT simulation technique with an arbitrarily shaped potential. The examples shown here are spectra of powder samples. Further analysis on monocrystals will give access to nondiagonal terms, as in works performed with the natural circular dichroism in XANES through the E1E2 interfering transition channel.[25] In XRS the monopole–dipole term, which we could call E0E1, offers new interesting perspectives to study samples without a center of symmetry using linearly polarized light. The work presented in this paper is also valid for electron energy loss spectroscopy (EELS), which is now routinely performed on many transmission electron microscopes, because it is based on the same transition operator. Finally, the code also contains a TD-DFT extension, which will be adapted to calculate the XRS response function of the L$_{23}$-edges of 3d transition elements.

■ AUTHOR INFORMATION

Corresponding Author
*E-mail: yves.joly@neel.cnrs.fr.

ORCID
Yves Joly: 0000-0002-1872-6112
Sergey A. Guda: 0000-0002-2398-1847

■ REFERENCES

(1) Schülke, W. In *Electron Dynamics by Inelastic X-Ray Scattering*; Chikawa, J., Helliwell, J. R., Lovesey, S. W., Eds.; Oxford University Press: New York, 2007.
(2) Sahle, C. J.; Mirone, A.; Niskanen, J.; Inkinen, J.; Krisch, M.; Huotari, S. Planning, performing and analyzing X-ray Raman scattering experiments. *J. Synchrotron Radiat.* **2015**, *22*, 400−409.
(3) Suzuki, T. X-Ray Raman Scattering Experiment. I. *J. Phys. Soc. Jpn.* **1967**, *22*, 1139−1150.
(4) Suzuki, T.; Nagasawa, H. X-Ray Raman Scattering. III. The Angular Dependence of the Scattering Intensity. *J. Phys. Soc. Jpn.* **1975**, *39*, 1579−1585.
(5) Cai, Y. Q.; Chow, P.; Chen, C. C.; Ishii, H.; Tsang, K. L.; Kao, C. C.; Liang, K. S.; Chen, C. T. Optical Design and Performance of the Taiwan Inelastic X-Ray Scattering Beamline (BL12XU) at SPring-8. *AIP Conf. Proc.* **2003**, *705*, 340−343.
(6) Fister, T. T.; Seidler, G. T.; Wharton, L.; Battle, A. R.; Ellis, T. B.; Cross, J. O.; Macrander, A. T.; Elam, W. T.; Tyson, T. A.; Qian, Q. Multielement spectrometer for efficient measurement of the

momentum transfer dependence of inelastic x-ray scattering. *Rev. Sci. Instrum.* **2006**, *77*, 063901.

(7) Verbeni, R.; Pylkkänen, T.; Huotari, S.; Simonelli, L.; Vanko, G.; Martel, K.; Henriquet, C.; Monaco, G. Multiple-element spectrometer for non-resonant inelastic X-ray spectroscopy of electronic excitations. *J. Synchrotron Radiat.* **2009**, *16*, 469−476.

(8) Sokaras, D.; Nordlund, D.; Weng, T.-C.; Mori, R. A.; Velikov, P.; Wenger, D.; Garachtchenko, A.; George, M.; Borzenets, V.; Johnson, B.; Qian, Q.; Rabedeau, T.; Bergmann, U. A high resolution and large solid angle x-ray Raman spectroscopy end-station at the Stanford Synchrotron Radiation Lightsource. *Rev. Sci. Instrum.* **2012**, *83*, 043112.

(9) Sahle, C. J.; Sternemann, C.; Schmidt, C.; Lehtola, S.; Jahn, S.; Simonelli, L.; Huotari, S.; Hakala, M.; Pylkkänen, T.; Nyrow, A.; Mende, K.; Tolan, M.; Hämäläinen, K.; Wilke, M. Microscopic structure of water at elevated pressures and temperatures. *Proc. Natl. Acad. Sci. U. S. A.* **2013**, *110*, 6301−6306.

(10) Soininen, J. A.; Ankudinov, A. L.; Rehr, J. J. Inelastic scattering from core electrons: A multiple scattering approach. *Phys. Rev. B: Condens. Matter Mater. Phys.* **2005**, *72*, 045136.

(11) Gordon, R.; Seidler, G. T.; Fister, T. T.; Haverkort, M. W.; Sawatzky, G. A.; Tanaka, A.; Sham, T. K. High multipole transitions in NIXS: Valence and hybridization in 4f systems. *Europhys. Lett.* **2008**, *81*, 26004.

(12) van Veenendaal, M.; Haverkort, M. W. Effective operator for $d − d$ transitions in nonresonant inelastic x-ray scattering. *Phys. Rev. B: Condens. Matter Mater. Phys.* **2008**, *77*, 224107.

(13) Hämäläinen, K.; Galambosi, S.; Soininen, J. A.; Shirley, E. L.; Rueff, J.-P.; Shukla, A. Momentum dependence of fluorine K-edge core exciton in LiF. *Phys. Rev. B: Condens. Matter Mater. Phys.* **2002**, *65*, 115111.

(14) Lehtola, J.; Hakala, M.; Sakko, A.; Hämäläinen, K. ERKALE− A flexible program package for X-ray properties of atoms and molecules. *J. Comput. Chem.* **2012**, *33*, 1572−1585.

(15) Sakko, A.; Hakala, M.; Soininen, J. A.; Hämäläinen, K. Density functional study of x-ray Raman scattering from aromatic hydrocarbons and polyfluorene. *Phys. Rev. B: Condens. Matter Mater. Phys.* **2007**, *76*, 205115.

(16) Bunău, O.; Joly, Y. Self-consistent aspects of x-ray absorption calculations. *J. Phys.: Condens. Matter* **2009**, *21*, 345501.

(17) Hämäläinen, K.; Manninen, S. Resonant and non-resonant inelastic x-ray scattering. *J. Phys.: Condens. Matter* **2001**, *13*, 7539−7555.

(18) Joly, Y.; Grenier, S. Theory of absorption near edge structure. In *X-Ray Absorption and X-Ray Emission Spectroscopy*; Bokhoven, J. A. V., Lamberti, C., Eds.; John Wiley & Sons: Chichester, U.K., 2016; Chapter 4, pp 73−97.

(19) Wood, J. H.; Boring, A. M. Improved Pauli Hamiltonian for local-potential problems. *Phys. Rev. B: Condens. Matter Mater. Phys.* **1978**, *18*, 2701−2711.

(20) Joly, Y. X-ray absorption near-edge structure calculations beyond the muffin-tin approximation. *Phys. Rev. B: Condens. Matter Mater. Phys.* **2001**, *63*, 125120.

(21) Bunău, O.; Joly, Y. Time-dependent density functional theory applied to x-ray absorption spectroscopy. *Phys. Rev. B: Condens. Matter Mater. Phys.* **2012**, *85*, 155121.

(22) Guda, S. A.; Guda, A. A.; Soldatov, M. A.; Lomachenko, K. A.; Bugaev, A. L.; Lamberti, C.; Gawelda, W.; Bressler, C.; Smolentsev, G.; Soldatov, A. V.; Joly, Y. Finite difference method accelerated with sparse solvers for structural analysis of the metal-organic complexes. *J. Phys.: Conf. Ser.* **2016**, *712*, 012004.

(23) Wyckoff, R. *Crystal Structures*; John Wiley: New York, 1963.

(24) Feng, Y.; Soininen, J. A.; Ankudinov, A. L.; Cross, J. O.; Seidler, G. T.; Macrander, A. T.; Rehr, J. J.; Shirley, E. L. Exciton spectroscopy of hexagonal boron nitride using nonresonant x-ray Raman scattering. *Phys. Rev. B: Condens. Matter Mater. Phys.* **2008**, *77*, 165202.

(25) Goulon, J.; Rogalev, A.; Wilhelm, F.; Goulon-Ginet, C.; Carra, P.; Marri, I.; Brouder, C. X-ray optical activity: Applications of sum rules. *J. Exp. Theor. Phys.* **2003**, *97*, 402−431.